

RES-NOVA: A revolutionary neutrino observatory based on archaeological lead

Luca Pattavina,^{1,2,*} Nahuel Ferreiro Iachellini,^{3,†} and Irene Tamborra^{4,‡}

¹*Physik-Department, Technische Universität München, 85747 Garching, Germany*

²*INFN, Laboratori Nazionali del Gran Sasso, 67100 Assergi, Italy*

³*Max-Planck-Institut für Physik, 80805 München, Germany*

⁴*Niels Bohr International Academy and DARK, Niels Bohr Institute, University of Copenhagen, Blegdamsvej 17, 2100, Copenhagen, Denmark*

(Dated: May 31, 2022)

We present the RES-NOVA project which will hunt neutrinos from core-collapse supernovae (SN) via coherent elastic neutrino-nucleus scattering (CE ν NS) using an array of archaeological lead (Pb) based cryogenic detectors. The high CE ν NS cross-section on Pb and the ultra-high radiopurity of archaeological Pb enable the operation of a high statistics experiment equally sensitive to all neutrino flavors with reduced detector dimensions and easy scalability to larger detector volumes. RES-NOVA will be operating in three phases with increasing detector volumes: (60 cm)³, (140 cm)³, and ultimately 15 \times (140 cm)³. It will be sensitive to SN bursts up to Andromeda with 5 σ sensitivity with already existing technology and will have excellent energy resolution with 1 keV threshold. Within our Galaxy, it will be possible to discriminate core-collapse SNe from black hole forming collapses with no ambiguity even in the first phase of RES-NOVA. The average neutrino energy of all flavors, the SN neutrino light curve, and the total energy emitted in neutrinos will be constrained with a precision of few % in the final detector phase. RES-NOVA will potentially detect the first flavor-blind neutrinos from the diffuse SN neutrino background with an exposure of 620 ton⁻¹ yr⁻¹. The RES-NOVA project has the potential to lay down the foundations for a new generation of neutrino telescopes, while relying on a very simple technological setup.

I. INTRODUCTION

Stars heavier than 8 M_{\odot} end their life giving birth to some of the most energetic transients in our Universe: core-collapse supernovae (SN) [1, 2]. Neutrinos play a major role in the SN mechanism [3]. During the SN explosion, 10⁵⁸ neutrinos are emitted; the detection of SN neutrinos would be enormously important to disclose information on the physics of the core collapse, not otherwise accessible [4–6]. Despite the steep progress in the field, many questions revolving around the SN mechanism remain unanswered. The detection of neutrinos from a SN burst occurring within our galaxy will also shed light on the yet poorly understood behavior of neutrinos at extreme densities [5–7] as well as on any non-standard neutrino properties [5, 8–15]. To maximize the amount of information that can be extracted from the neutrino signal and precisely reconstruct the neutrino emission properties, it will be crucial to detect all six neutrino flavors [16–18].

Existing neutrino detectors with large target mass [$\mathcal{O}(10$ kton)] are sensitive to SN neutrinos, in addition to others being planned or under construction [5, 19]. Astrophysical neutrinos can be detected via weak charge-current (CC) and neutral-current (NC) interactions on protons and electrons. The most significant interaction processes are inverse-beta decay (IBD) and elastic scattering on electrons (ES).

The IBD requires target material elements such as water or organic scintillators, where a large number of free protons is available. This channel is sensitive to $\bar{\nu}_e$, and experiments usually detect the positron annihilation. A measurement of the positron energy can lead to a precise estimation of the SN neutrino energy. This is the case of KamLAND [20], Borexino [21] and LVD [22] that are using large volume organic liquid scintillators. In addition, JUNO [23], which is under commissioning, will be online within the next few years from now with an extremely large detector mass of 20 kton.

Super-Kamiokande [24] runs a large volume water Cherenkov detector of 32 kton. Thanks to its recent upgrade, where gadolinium was dissolved into water, the neutrino interaction signal (IBD of $\bar{\nu}_e$) can be tagged with a higher efficiency (90% [25]) via neutron capture on gadolinium. This additional feature has the potential to strongly improve the sensitivity of Super-Kamiokande to SN neutrino interactions, especially for what concerns the detection of the diffuse background of SN neutrinos (DSNB). The IceCube Neutrino Telescope [26] is a Cherenkov detector in ice with the potential to provide the largest statistics of SN neutrino events. On the other hand, the upcoming liquid argon facility DUNE will allow to detect ν_e 's with higher statistics [27].

The ES is also a relevant detection channel for SN neutrinos, being sensitive to all neutrino flavors through NC interactions (while the CC channel is exploitable for $\bar{\nu}_e$ and ν_e as well). Unfortunately, in conventional detectors the ES has an interaction cross-section which is some orders of magnitude lower than IBD and it can contribute for a few percents to the total SN event rate [28]. Other detection channels may also be used, such as CC in-

* luca.pattavina@lngs.infn.it

† ferreiro@mpp.mpg.de

‡ tamborra@nbi.ku.dk

interactions on nuclei [16] or protons [17, 29]. However, these processes – especially the interactions on nuclei – have much lower cross-sections. Furthermore, they are affected by large theoretical uncertainties and lack of experimental data at the energy scale of interest. This is the case of lead or iron targets proposed for SN neutrino detection via inelastic neutrino-nucleus CC interactions [30–32].

In this picture, the available experimental approaches lack of a detection channel equally and highly sensitive to all neutrino flavors.

The coherent elastic neutrino-nucleus scattering (CE ν NS) is an especially intriguing option thanks to its sensitivity to all neutrino flavors (NC process) and its high interaction cross section. The latter scales as the square of the neutron number of the target nucleus at low energies [33, 34].

In the context of SN neutrino detection, CE ν NS detectors would allow an estimation of the overall neutrino emission properties without the uncertainties related to standard oscillation physics [5]. In addition, CE ν NS-based detectors complement dedicated neutrino telescopes, allowing to potentially improve our chances to reconstruct the emission properties of the non-electron (anti)neutrinos. Direct detection dark matter experiments exploit CE ν NS [35] and can also act as neutrino telescopes, if the target material is larger than a few tons [18, 36–40].

In this paper, we propose a revolutionary approach for the detection of SN neutrinos: the archaeological lead (Pb) cryogenic detector RES-NOVA. RES-NOVA will exploit CE ν NS for the detection of astrophysical neutrinos. Lead is the only element of the periodic table that simultaneously offers the highest CE ν NS cross-section, for a high interaction rate, and the highest nuclear stability, for ultra-low background levels. The proposed detector would allow to obtain high statistics of neutrino events through CE ν NS by employing a detector with a miniaturized volume, compared to the currently running ones. Furthermore, the employment of archaeological Pb will secure a background level which will be some orders of magnitude lower than other Pb samples, thus enabling a high statistical significance detection of SN neutrinos. The high CE ν NS cross section of Pb, the ultra-low background of archaeological Pb and the cutting-edge performance of solid state cryogenic detectors, will allow the proposed experiment to reach out to SNe up to $\mathcal{O}(1)$ Mpc and with the potential to reconstruct the neutrino average energy with an uncertainty of few %.

The structure of the paper is as follows. Section II provides a brief introduction on the neutrino emission properties from the six benchmark SN models adopted in this work. We discuss the potential of exploiting CE ν NS in a lead-based cryogenic detector, introduce the main characteristics of our proposed technology, and discuss the expected backgrounds and the detector energy response in Sec. III. The event rate for a Galactic SN is estimated in Sec. IV; we also explore the possibility of distinguish-

ing among different SN models and nuclear EoS, and reconstruct the average energy of the SN neutrinos. The possibility of detecting the DSNB with RES-NOVA is explored in Sec. V. Finally, conclusions are presented in Sec. VI.

II. NEUTRINO EMISSION FROM CORE-COLLAPSE SUPERNOVAE AND BLACK HOLE FORMING COLLAPSES

For a SN at distance d from the Earth (assumed to be $d \simeq 10$ kpc for a Galactic burst), the differential flux for each neutrino ν_β (ν_e , $\bar{\nu}_e$, and $\nu_x = \nu_{\mu,\tau}, \bar{\nu}_{\mu,\tau}$) at the time t after the SN core bounce is

$$f_\beta^0(E, t) = \frac{L_\beta(t)}{4\pi d^2} \frac{\phi_\beta(E, t)}{\langle E_\beta(t) \rangle}, \quad (1)$$

with $L_\beta(t)$ being the time-dependent neutrino luminosity and $\langle E_\beta(t) \rangle$ the ν_β mean energy. The neutrino energy distribution $\phi_\beta(E, t)$ is parametrized as [41, 42]:

$$\phi_\beta(E, t) = \xi_\beta(t) \left(\frac{E}{\langle E_\beta(t) \rangle} \right)^{\alpha_\beta(t)} \exp \left(-\frac{(\alpha_\beta(t) + 1)E}{\langle E_\beta(t) \rangle} \right), \quad (2)$$

where $\alpha_\beta(t)$ is such that

$$\frac{\langle E_\beta(t)^2 \rangle}{\langle E_\beta(t) \rangle^2} = \frac{2 + \alpha_\beta(t)}{1 + \alpha_\beta(t)}, \quad (3)$$

and $\xi_\beta(t)$ is obtained by $\int dE \phi_\beta(E, t) = 1$.

In order to estimate the event rate expected in RES-NOVA, we rely on the neutrino emission properties from a set of one-dimensional (1D) spherically symmetric hydrodynamical SN simulations by the Garching group [5, 43]. In order to take into account the variability of the expected neutrino signal as a function of the SN evolution outcome (i.e. standard core-collapse SNe and black hole forming stellar collapses also dubbed failed SNe in the following), SN mass, and nuclear equation of state (EoS), we adopt six different SN models. Four models of standard core-collapse SNe with mass of 9.6 and 27 M_\odot , each model with Lattimer and Swesty EoS [44] with nuclear incompressibility modulus $K = 220$ MeV (LS220 EoS) and with the SFHo hadronic EoS (SFHo EoS) [45]. The remaining two models are black hole forming collapses with a mass of 40 M_\odot : s40c and s40s7b2c, corresponding to “slow” and “fast” black hole formation (i.e. with different mass accretion rate) [5]. Both black hole forming models have been simulated with LS220 EoS.

The resultant temporal evolution of the neutrino flux introduced in Eq. 1 summed over all six flavors, for $d = 10$ kpc, and for the six benchmark SN models (CC-SN) on the left and for the black hole stellar collapses (failed SN) on the right. As visible from the left panel of Fig. 1, the neutrino signal lasts for $\mathcal{O}(10)$ s,

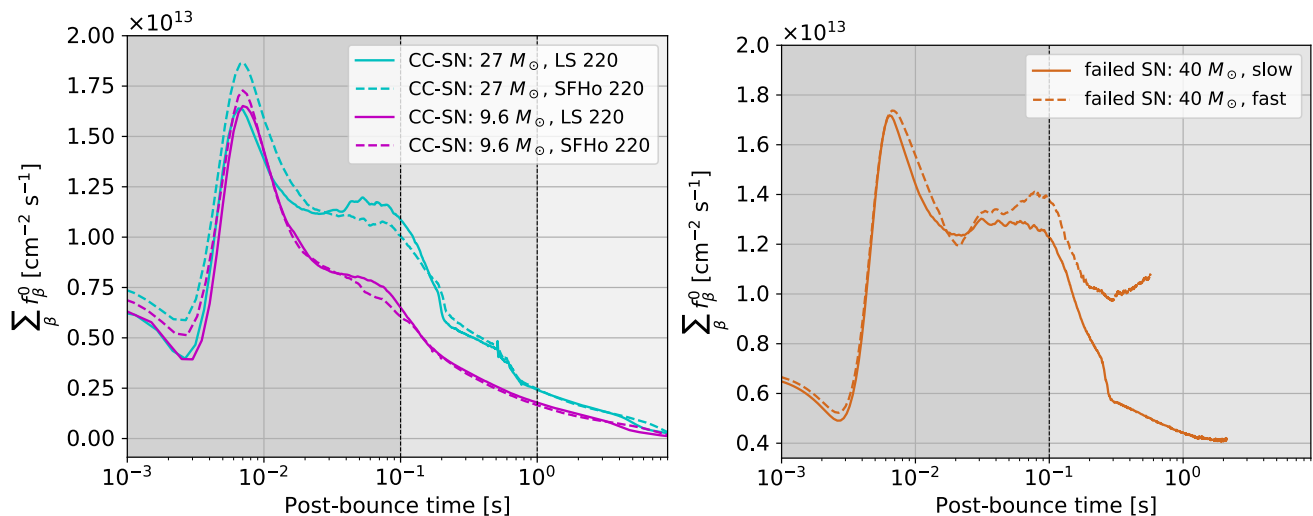


FIG. 1. Temporal evolution of the total neutrino flux (defined as in Eq. 1 for each ν_β and summed over all six neutrino flavors) for a stellar collapse occurring at 10 kpc. *Left panel:* Neutrino fluxes for our benchmark 9.6 and 27 M_\odot core-collapse SN models with LS220 and SFHo EoSs. The three shaded regions highlight the neutronization burst, the accretion phase, and the Kelvin-Helmholtz cooling phase, from left to right respectively. *Right panel:* Neutrino fluxes for our 40 M_\odot black hole forming collapses with slow and fast accretion (slow and fast failed SN, respectively). The black hole formation suddenly halts the neutrino signal.

but it drops considerably after a few seconds. As highlighted by the gray-shaded regions, the overall neutrino signal can be divided in three time windows: the neutronization burst, the accretion phase, and the Kelvin-Helmholtz cooling phase. The neutronization burst originates as the shock wave is moving outwards through the iron core and free protons and neutrons are produced due to iron dissociation. The rapid electron capture by nuclei and free protons is responsible for generating a ν_e burst lasting for about ~ 0.05 s. In this phase, the neutrino signal is mildly dependent on the SN mass and nuclear EoS [$\mathcal{O}(1 - 10\%)$] [46].

The neutronization burst is followed by the accretion phase lasting until ~ 1 s. The shock after losing all its energy by dissociating iron nuclei stalls, and neutrinos are thought to provide fresh energy to the shock to finally revive it and trigger the explosion according to the delayed neutrino heating mechanism. This eventually leads to the explosion after few hundreds of milliseconds.

After, the Kelvin-Helmholtz phase occurs. As the newly born proto-neutron star cools and deleptonizes, the neutrino flux gradually decreases and the neutrino emission properties tend to become similar across all flavors. Section 2.4.6 of Ref. [5] provides a detailed description of the dependence of the neutrino emission properties from the EoS. However, one can notice that the dependence of the neutrino fluxes from the EoS is weaker than their dependence on the progenitor mass.

The right panel of Fig. 1 shows the neutrino flux expected from failed SNe for comparison. The first clear difference between the two SN subsets is the duration of the neutrino signal. Black hole formation halts the neutrino emission after 0.57 s for the model s40s7b2c (fast

failed SN) and after 2.1 s for the model s40c (slow failed SN). Moreover, the latter model displays lower mass accretion rate (see Ref. [5] for more details).

It is worth noticing that 1D SN models describe the overall neutrino emission properties well, but do not carry signatures of the hydrodynamical instabilities that may affect the neutrino signal during the accretion rate, see e.g. Refs. [3, 47, 48]. However, in this work, we are interested in reconstructing the general properties of the SN neutrino burst, and neglect any small-scale feature affecting the neutrino signal.

The total flux summed over six flavors in Fig. 1 is insensitive to flavor conversions. However, neutrinos change their flavor while they propagate through the stellar envelope as well as on their way to Earth. In the proximity of the SN core, the neutrino density is so high that neutrino-neutrino interactions are believed to be dominant giving rise to non-linear effects in the flavor evolution history. At larger radii, neutrinos undergo Mikheev-Smirnov-Wolfenstein (MSW) resonant conversions because of interactions with the matter background. Turbulences or large stochastic fluctuations of the matter density in the SN envelope can affect the neutrino flavor distribution. We refer the reader to Refs. [5, 6, 49] for recent reviews on the topic and references therein.

The total neutrino flux summed over all six flavors may still be affected by non-standard physics. This is the case of heavy and light sterile neutrinos [9, 10, 12], secret neutrino interactions [8, 50], neutrino decay [13, 51], beyond the Standard Model light particles [11], and non-standard neutrino interactions [14, 15]. Exploiting CE ν NS as another detection channel for SN neutrinos may open a new portal for probing the Standard Model.

III. NEUTRINO DETECTION IN A LEAD-BASED CRYOGENIC DETECTOR

In this Section, we focus on the intrinsic potential of exploiting CE ν NS in a lead-based cryogenic detector and introduce the main features of our proposed neutrino telescope RES-NOVA. A brief overview of the expected backgrounds and the detector energy response is also provided.

A. Coherent elastic neutrino-nucleus scattering in a lead-based cryogenic detector

CE ν NS is a NC process, equally sensitive to all neutrino flavors. This feature makes CE ν NS a complementary approach to other conventional techniques for neutrino detection which are instead mostly sensitive to $\bar{\nu}_e$ or ν_e . In addition, as already pointed out in [16], CE ν NS offers a wealth of applications in neutrino physics being a threshold-less process, thus sensitive to the full SN neutrino signal [18, 36].

The interaction cross-section of CE ν NS can be easily computed by Standard Model basic principles for all neutrino energies and it has been measured experimentally recently [34]. The cross-section is [33]:

$$\frac{d\sigma}{dE_R} = \frac{G_F^2 m_N}{8\pi(\hbar c)^4} [(4\sin^2 \theta_W - 1)Z + N]^2 \left(2 - \frac{E_R m_N}{E^2}\right) \cdot |F(q)|^2, \quad (4)$$

where G_F is the Fermi coupling constant, θ_W the Weinberg angle, Z and N the atomic and neutron numbers of the target nucleus, while m_N its mass, E the energy of the incoming neutrino and E_R the recoil energy of the nucleus. The last term of the equation, $F(q)$, is the elastic nuclear form factor at momentum transfer $q = \sqrt{2E_R m_N}$. It represents the distribution of the weak charge within the nucleus and for small momentum transfers its value is close to unity. The parameterization of $F(q)$ follows the model of Helm [52]; for an exact evaluation of $F(q)$ see [53].

Elastic neutrino scattering on Pb nuclei is coherent, if the energy of the incoming particles is $E \lesssim 30$ MeV. For this reason, Pb can be considered an efficient target for SN neutrinos, although SN neutrinos may have higher energies ([1, 50] MeV, see Sec. II). For the sake of accuracy, we also take into account possible non fully-coherent interactions through the evaluation of $F(q)$ for different momentum transfers. It is worth mentioning that having a target nucleus with high N increases the cross-section, and if the interaction is coherent we have a further enhancement: $\sigma_{\text{CE}\nu\text{NS}} \propto N^2$.

Figure 2 displays the CE ν NS cross-section for different nuclei frequently used for the realization of neutrino detectors. From an experimental point of view, Pb is the best target candidate to be used for neutrino detection via CE ν NS thanks to the high N , thus high

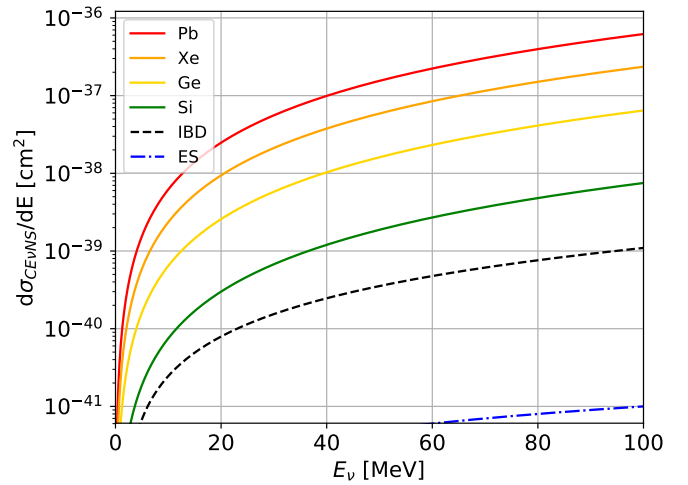


FIG. 2. Coherent elastic neutrino-nucleus scattering (CE ν NS) cross sections as a function of the energy of the incoming neutrino for different target nuclei. The dashed lines show the inverse-beta decay (IBD) and neutrino elastic scattering on electrons (ES) cross-sections for comparison. Given the high cross-section, CE ν NS has the potential to provide large statistics with small detector volumes.

cross-section, and its nuclear stability, intrinsic low backgrounds [54]. Furthermore, CE ν NS has an interaction cross-section much higher than the conventional IBD and ES channels. CE ν NS is about four orders of magnitude greater than other NC processes, namely ES. This is a great advantage for detectors exploiting CE ν NS, in fact they can potentially achieve higher statistics with smaller detector volumes.

The signature produced by astrophysical neutrinos interacting on Pb via CE ν NS is the nuclear recoil of few keV of energy. In order to evaluate the time and energy distribution of the neutrino induced events we compute the differential scattering rate in the detector. This is done by integrating the product of the total neutrino flux (Eq. 1) and the CE ν NS differential interaction cross-section (Eq. 4) over the relevant incident neutrino energy range, and by multiplying the resulting function for the total number of target nuclei (N_{Pb}):

$$\frac{d^2 R}{dE_R dt} = \sum_{\alpha} N_{\text{Pb}} \int_{E_{\min}} f_{\alpha}^0(E, t) \frac{d\sigma}{dE_R} dE, \quad (5)$$

where the sum is over all six neutrino flavors.

The best available experimental technique for the detection of keV nuclear recoils in Pb-based detectors is the cryogenic one [54]. Low temperature cryogenic detectors will bring, for the first time in a neutrino telescope, the following unique features:

- fully active volume. The entire detector is sensitive to particle interactions, and no volume fiducialization is needed, unlike all other adopted technologies (e.g., water Cherenkov detectors, noble-liquid TPCs);

- per-mille energy resolution over a wide energy range [55–57], from few eV up to some MeV, allowing the identification of any structure in SN neutrino recoil spectra;
- scalability to large detector volumes [58];
- operation of different detector compounds [54, 59–61], without being limited by the technology to a single compound (e.g. water, liquid-Ar/Xe).
- active background suppression techniques, such as scintillating compounds for particle identification (e.g. e^-/γ , α , neutrons) [54, 62].

For the realization of the RES-NOVA detector different crystal absorbers are taken into consideration: pure Pb crystals or Pb containing crystals, as PbWO_4 or PbMoO_4 . These crystals were already operated as cryogenic calorimeters with excellent performance [54, 63, 64].

In order to show the potential of the proposed Pb-based cryogenic detector technology, in the following we will consider the $27 M_\odot$ model with LS220 EoS as our *reference SN model*. This will be used for the estimation of the optimal detector parameters, namely energy threshold and detector volume (mass). We will focus only on the initial 10 s of the neutrino signal after the core bounce.

Figure 3 shows the integrated total number of detected events ($\int d^2R/(dE_R dt)dE_R dt$) for different detector energy thresholds as a function of the detector linear dimension. A detector with linear dimensions of tens of cm can achieve similar sensitivity (comparable number of detected events) to $\mathcal{O}(\text{kton})$ detectors. With the additional advantage that the proposed Pb detector is equally sensitive to all neutrino flavors.

As shown in the secondary (top) x-axis of Fig. 3, the high density of Pb allows to achieve large detector masses with small detector volumes. Thus, the proposed technology has a great potential for detector upgrades to larger volumes.

The RES-NOVA research program will be divided in three main phases (see Tab. I), with increasing detector volumes and sensitivities. In Fig. 3, the two initial phases of the program are highlighted by two markers. In the first phase, the RES-NOVA detector will be able to detect about 100 SN neutrino events with a total detector volume of $(60 \text{ cm})^3$ and an energy threshold of only 1 keV. For the sake of comparison, for a similar SN event, Super-Kamiokande would observe 230 events exploiting NC-ES reactions [25]. The second phase foresees a detector scaling to $(140 \text{ cm})^3$ of the total volume without any other technological advancement; the third phase would consist in installing multiple $(140 \text{ cm})^3$ detectors in 15 different sites. Table I summarizes the main detector characteristics of the RES-NOVA research program.

In summary, running a Pb based cryogenic detector employing $\text{CE}\nu\text{NS}$ will be of great importance given the high $\text{CE}\nu\text{NS}$ interaction cross-section and advantages of

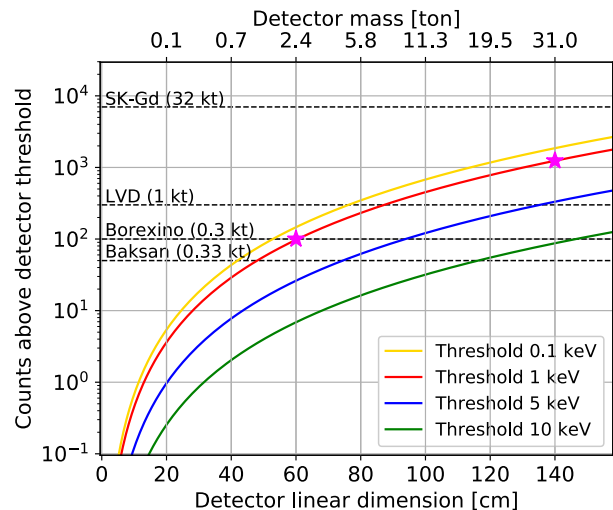


FIG. 3. Number of events for different linear dimensions (or effective mass) of the detector and different energy thresholds for our benchmark $27 M_\odot$ SN model with LS220 EoS integrated over 10 s after the core bounce. The horizontal lines represent the signal observed in dedicated neutrino observatories for the same SN input [28]; in parenthesis the respective detector masses are shown. A Pb-based detector with linear dimensions of tens of cm can achieve a number of detected events similar to $\mathcal{O}(\text{kton})$ flavor-dependent detectors. The two markers at 60 cm and 140 cm represent the sensitivity of the two first phases of the RES-NOVA project for our fiducial energy threshold.

the cryogenic technique. This innovative approach has the potential to allow an important downsizing of the overall experimental volume, enabling future upgrades of the set-up for higher sensitivities. As we will discuss in the next Section, this is possible only if high-purity archaeological Pb is employed and if the Pb detectors are operated as low temperature calorimeters.

B. RES-NOVA detector design

The RES-NOVA detector has a modular design. This ensures a fast and effective detector upgrade, without the need of specific technological improvements. In the first phase (RES-NOVA Phase-1, RN^1), the detector has a

TABLE I. Detector characteristics for the three phases of the RES-NOVA research program, see main text for more details. The background index column refers to the background in the 1–40 keV region of interest.

	Linear dimension	Detector mass	Energy threshold	Background index
RN-1	60 cm	2.4 t	1 keV	0.1 c/keV/t/10 s
RN-2	140 cm	31 t	1 keV	0.1 c/keV/t/10 s
RN-3	15 × 140 cm	465 t	1 keV	0.1 c/keV/t/10 s

volume small enough to fit in the commercially available cryogenic infrastructures, and it consists of 500 detectors with total linear dimension of the array of 60 cm. A preliminary design of the RN¹ experimental apparatus is sketched in Fig. 4. The second phase (RES-NOVA Phase-2, RN²) is expected to replicate the RN¹ design for ~ 12 times and should fit inside a larger experimental facility, similar to the one currently operated by CUORE [65], the largest cryogenic infrastructure for low temperature detectors. The infrastructure will host 6000 crystals with total linear dimension of 140 cm. Finally, the ultimate phase of this research program (RES-NOVA Phase-3, RN³) foresees 15 detectors, with technical features similar to the ones of RN², installed in deep-underground laboratories world-wide, creating a Pb-based network of SN neutrino observatories.

We foresee to operate detectors with an energy threshold of 1 keV, which is within the reach with the available technologies. The current lowest energy thresholds achieved with low temperature detectors are at the level of tens of eV, as demonstrated by the CRESST [55], the EDELWEISS [66] and CDMS [67] experiments. Large arrays of cryogenic detectors were already shown to be feasible, as demonstrated by the CUPID-0 [68] and the CUORE [58] experiments, running respectively 57 and 988 calorimeters.

The technology proposed for the realization of RES-NOVA is already in place. Nevertheless, the effective feasibility of merging all the necessary technologies in one single experiment needs to be demonstrated. In order to show the potential of the RES-NOVA research program, in the following, we will forecast the expected background level and SN neutrino event rate in a lead-based detector.

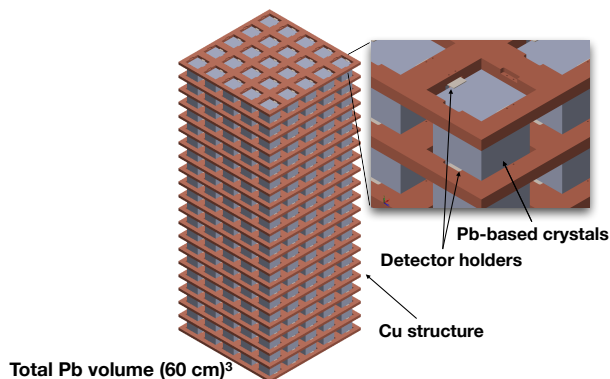


FIG. 4. Schematic drawing of the Phase-1 detector, total volume $(60 \text{ cm})^3$. The detector is composed by 20 floors of 25 crystals each, arranged in a tightly packed configuration. Copper is used, at the same time, as detector holding structure and thermal bath for the detector cool-down. The inset shows a zoom-in of the detector single module.

C. Expected backgrounds

In the field of cryogenic detectors for rare event investigations [69], the main limitation to the experimental sensitivity is the background produced by cosmic-rays induced particles (e.g. neutrons) and the detector intrinsic radiopurity, namely the concentration of $^{235/238}\text{U}$ and ^{232}Th decay chain products in the absorber. While the first background source can easily be mitigated or suppressed by installing the experimental set-up in deep underground laboratories and equipping them with highly efficient vetoes, the second one needs a different approach. The materials that should be used for the detector realization should be selected for their intrinsic radiopurity. For this reason, a thorough screening of the concentration of $^{235/238}\text{U}$ and ^{232}Th decay chain radionuclides is mandatory before the detector realization.

As already mentioned, Pb is the ideal element to be used as detector target for the detection of $\mathcal{O}(10 \text{ MeV})$ neutrinos. Unfortunately, the main background source in Pb containing detectors is ^{210}Pb . This is a natural radioactive isotope produced by the ^{238}U decay chain. It has a half-life of 22.3 yr and it β^- decays with a low energy Q-value of 63 keV, exactly around our region of interest (RoI). For these reasons, ^{210}Pb is considered to be the most dangerous isotope when investigating low-energy rare events (e.g. dark matter searches and CE ν NS related searches). Whenever ^{210}Pb contaminates a detector (whether it is a cryogenic one or not), it can only be partially removed by means of advanced cleaning and purification techniques [70, 71].

Here, we propose to overcome all these issues by running a detector made of archaeological Pb. If the age of Pb is old enough (e.g. Roman Pb is more than 2000 yr old) the concentration of ^{210}Pb , and its decay products, is strongly suppressed. The outstanding radiopurity of an archaeological Roman Pb cryogenic detector has been recently demonstrated in Ref. [63]. There, the lowest limit on the concentration of ^{210}Pb in archaeological Pb samples was measured: $< 2.5 \times 10^{-18} \text{ g/g}$ ($< 715 \mu\text{Bq/kg}$), 4-orders of magnitude better than any other low-radioactivity Pb sample [63]. The concentration of other radio-nuclides in archaeological Pb, namely $^{235/238}\text{U}$ and ^{232}Th , was also investigated in other works; also the concentration of these radio-nuclides was found to be extremely low: $< 10^{-12} \text{ g/g}$ [72].

The sensitivity of an archaeological Pb-based cryogenic detector to SN neutrinos is shown in Fig. 5. The detector energy response to the SN *reference signal* (27 M_\odot model with LS220 EoS at 10 kpc) is shown. The detector counting rate, normalized per detector unit mass and for a neutrino signal duration of 10 s, is plotted as a function of the recoil energy measured by the detector. In the same plot, the expected background level from a conventional low-background Pb [73] and from an archaeological Pb [63] sample are also shown. A detection of SN neutrinos statistically significant is possible only if archaeological Pb is employed for the detector realization.

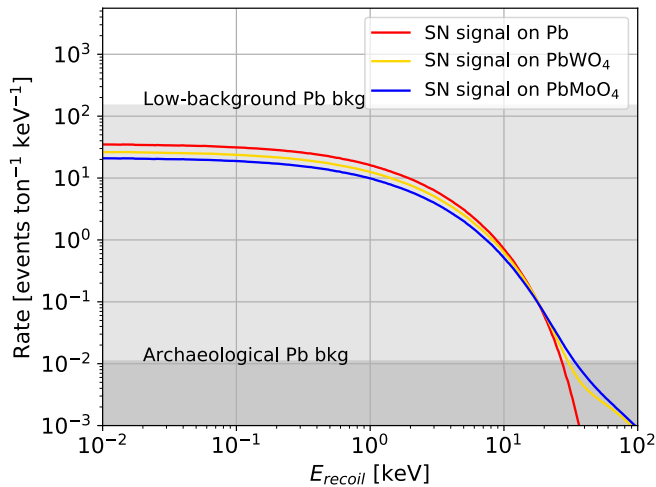


FIG. 5. Expected total number of SN neutrino events as a function of the recoil energy for a SN burst at 10 kpc in a detector made of Pb (in red), PbWO₄ (in yellow) and PbMoO₄ (in blue). The all-flavor and time-integrated neutrino signal for the 27 M_{\odot} SN model with LS220 EoS has been adopted as input. The light and dark grey areas represent the expected background levels induced by low-background Pb [73] and by archaeological Pb [63], respectively.

tion. This ensures an outstanding signal-to-noise ratio in the entire RoI.

The potential of this new approach (ultra-low background, fully-active detector and high interaction cross-section) is demonstrated by the detector miniaturization. In fact, even a detector with linear dimensions of about 40 cm (equivalent to 1 ton of mass), the SN neutrino signal would be about 3-orders of magnitude higher than the expected background.

D. Detector energy response

The detector energy response to a time-integrated SN signal and the expected background are shown in Fig. 5.

We assumed as detector energy resolution of 0.2 keV¹ over the entire RoI.

The advanced detector performance is achievable thanks to the extremely low energy of the information carriers in solid state cryogenic detectors, which are phonons with energy of few μeV . The energy distribution of the phonons depends on the operating temperature of the detector, which in our case is $\mathcal{O}(\text{mK})$. The energy deposited in the absorber by one neutrino interaction is of the order of few keV. So for a single neutrino interaction about 10^9 phonons are generated in the detector.

¹ We conservatively assume the detector energy resolution to be 1/5 of the detector energy threshold: $E_{\text{thr}} = 5 \sigma$. Thus, if $E_{\text{thr}} = 1 \text{ keV}$, $\sigma = 0.2 \text{ keV}$

The small statistical and thermodynamic fluctuations of the system allow to achieve an energy resolution at the permil scale over a broad energy range. This experimental approach makes possible the operation of almost ideal calorimeters able to measure the entire energy deposited in the detector irrespectively of the type of interacting particle and with very limited uncertainties related to the energy reconstruction (e.g., nuclear recoil quenching).

The detector response for the three compounds considered (pure Pb, PbWO₄ and PbMoO₄) is shown in Fig. 5. There is no relevant difference in the detector counting rates for the different compounds, except for the higher energy component. Compounds containing oxygen feature a higher energy tail of the SN signal, due to the lightness of the element, hence higher transferred momenta. For the sake of simplicity, in the following we will only consider a detector made of pure Pb crystals.

IV. RECONSTRUCTION OF THE NEUTRINO EMISSION PROPERTIES FOR A GALACTIC BURST

In this Section, we explore the possibility of detecting a SN in our Galaxy through a lead-based cryogenic detector. We focus on the reconstruction of the neutrino signal as a function of time and discuss the potential of distinguishing among different SN models and nuclear EoS. After reconstructing the average energy of SN neutrinos from the detected signal, we also estimate the total energy emitted in neutrinos. At last, we discuss the SN neutrino detection significance of RES-NOVA for extra-galactic bursts.

A. Reconstruction of the supernova neutrino light curve

A Galactic SN will be a once-in-a-lifetime opportunity. Hence, we should be able to extract as much as possible information from the burst. We compute the expected counting rate of the RES-NOVA detectors as a function of time by integrating Eq. 5 with respect to E_R over the RoI, from the detector energy threshold to 40 keV. Furthermore, the computed dR/dt is smeared according to the detector time resolution, which is conservatively assumed to be 100 μs . The detector response to the different SN models in Fig. 1 is shown in Fig. 6. The detector counting rate is normalized per detector mass unit, thus it is sufficient to multiply the rate for each RES-NOVA detector mass to compute the expected total number of SN neutrino events as a function of time.

The main spectral features of Fig. 1 also appear in Fig. 6. All the models show the neutronization peak at $\sim 10 \text{ ms}$, followed by a decrease of the detector counting rate. The only exception is the fast failed SN model characterized by an increasing counting rate. The RES-NOVA technology, even in its first stage, is able to clearly

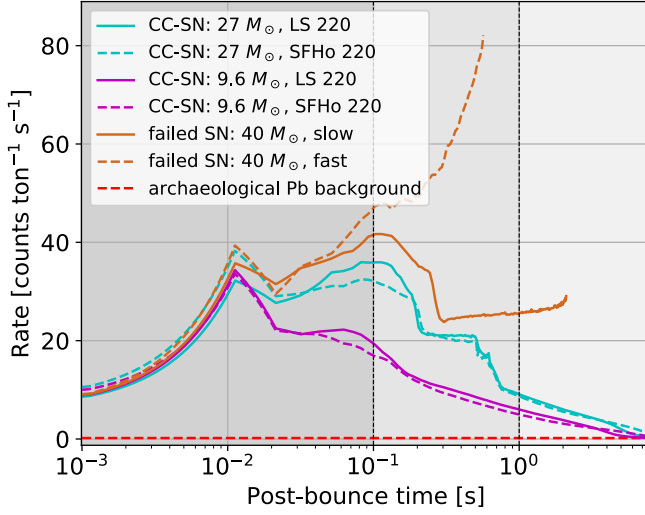


FIG. 6. Differential recoil rate integrated over the recoil energy as a function of the post-bounce time per unit of detector mass for six SN models. The time profile of the event rate is convolved with the detector time response. The gray shadowed regions mark the three different phases of the SN neutrino signal (neutronization burst, accretion phase, and cooling phase). The event rates of different SN models are easily distinguishable from each other, although there is a smaller variation of the expected rate due to the nuclear EoS.

identify the type of SN event (i.e., core-collapse or failed burst) by looking at the time distribution of the detector counting rate, namely the last bin which shows a neutrino event.

In order to precisely estimate the SN mass and EoS, a high statistics of neutrino events is crucial. For this reason, the larger is the RES-NOVA detector mass the more information will be retrieved. This is the focus of the next section.

B. Supernova model discrimination

We now investigate the potential of a cryogenic Pb-detector to distinguish between the six different SN models considered in this work, by relying on the different time evolution of the related neutrino lightcurve (see Fig. 6). We determine the total number of expected events by integrating dR/dt over the relevant post-bounce time interval:

$$N_{\text{exp}} = \int \frac{d^2 R}{dE_R dt} dt dE_R = \int \frac{dR}{dt} dt, \quad (6)$$

and the probability density function for an event to occur at the time t :

$$p(t) = \frac{1}{N_{\text{exp}}} \frac{dR}{dt}. \quad (7)$$

Thanks to Eqs. 6 and 7, we can generate Monte Carlo experiments (mock-up data) for the different SN models

and detector masses. Equation 6 is used to randomly determine the number of observed events N_{obs} from a Poissonian distribution with expectation value $\lambda = N_{\text{exp}}$ for each simulated experiment. The time occurrence of each event, t_i , is drawn from the probability density function described in Eq. 7, then it is randomized with the assumed detector's time resolution of 100 μs .

The capability of the cryogenic detector to discriminate among the different models is investigated through the likelihood \mathcal{L} :

$$\ln \mathcal{L} = N_{\text{obs}} \ln N_{\text{exp}} - N_{\text{exp}} + \sum_{i=1}^{N_{\text{obs}}} \ln p(t_i) \quad (8)$$

For one given detector mass and SN model j , we compute $\ln \mathcal{L}^j$ over a simulated dataset. The value of $\ln \mathcal{L}^j$ for the j th-model is assigned as a score of the model to the dataset. If the best scoring model for a dataset was the one used to generate that dataset, then we conclude that we successfully reconstructed the model.

We generated 10^4 different experiments for each SN model and evaluated the likelihood according to Eq. 8. The results on the probability to reconstruct the exact SN model from the simulated experiments are summarized in Tab. II. The table shows how well each phase of the RES-NOVA detector will be able to pin down the SN models considered in this work. The RN¹ detector can state without ambiguity whether the SN event led to the formation of a black hole or a neutron star, some information about the SN mass can also be inferred. On the other hand, the RN² detector can identify the progenitor mass and the nuclear EoS of the model with an accuracy $> 90\%$. Finally, RN³ has the outstanding potential to uniquely identify each of the model taken into account.

C. Estimation of the neutrino spectral features and total energy emitted in neutrinos

The relevant astrophysical parameters that we can extract from the all-flavor neutrino signal are the average neutrino energy and the neutrino flux amplitude. In order to assess these two parameters, we adopt the following parametrization for the time-integrated neutrino flux summed over all flavors along the lines of Eq. 1 [36]:

$$f^0(E; \langle E \rangle, \alpha_T) = \sum_{\beta} \int_{t_1}^{t_2} f_{\beta}^0(E, t) dt = A_T \xi_T \left(\frac{E}{\langle E \rangle} \right)^{\alpha_T} \exp \left(-\frac{(1+\alpha_T)E}{\langle E \rangle} \right), \quad (9)$$

where

$$\xi_T(\alpha_T, \langle E \rangle) = \frac{\left(\frac{\alpha_T+1}{\langle E \rangle} \right)^{\alpha_T+1} \langle E \rangle^{\alpha_T}}{\Gamma(\alpha_T+1)}$$

is such that $\int dE f^0(E) = 1$, A_T is the time-integrated neutrino flux at the detector site, and $\langle E \rangle$ is the all-flavor

TABLE II. Probability to identify the SN model by means of a maximum-likelihood analysis of the expected time distribution of the neutrino signal in the detector (see Fig. 6). The values in $()$, $[]$ and $\{\}$ refer to the three RES-NOVA phases: RN¹, RN² and RN³, respectively.

		Reconstructed SN model					
		40 M_\odot - slow	40 M_\odot - fast	9.6 M_\odot - SFHo	9.6 M_\odot - LS220	27 M_\odot - SFHo	27 M_\odot - LS220
True SN model	40 M_\odot - slow	(1) [1] {1}	(0) [0] {0}	(0) [0] {0}	(0) [0] {0}	(0) [0] {0}	(0) [0] {0}
	40 M_\odot - fast	(0.001) [0] {0}	(0.997) [1] {1}	(0) [0] {0}	(0.001) [0] {0}	(0) [0] {0}	(0.001) [0] {0}
	9.6 M_\odot - SFHo	(0) [0] {0}	(0.001) [0] {0}	(0.396) [0.926] {1}	(0.178) [0.003] {0}	(0.275) [0.051] {0}	(0.151) [0.020] {0}
	9.6 M_\odot - LS220	(0.001) [0] {0}	(0.007) [0] {0}	(0.113) [0.005] {0}	(0.614) [0.931] {1}	(0.056) [0.001] {0}	(0.209) [0.064] {0}
	27 M_\odot - SFHo	(0) [0] {0}	(0) [0] {0}	(0.256) [0.058] {0}	(0.046) [0] {0}	(0.520) [0.939] {1}	(0.179) [0.003] {0}
	27 M_\odot - LS220	(0) [0] {0}	(0) [0] {0}	(0.115) [0.002] {0}	(0.228) [0.010] {0}	(0.139) [0.005] {0}	(0.518) [0.982] {1}

average energy. With such a parametrization the neutrino energy spectrum is fully described by $\langle E \rangle$, A_T and α_T . The latter is approximated with its time-average, over the $[t_1, t_2]$ time interval (corresponding to the neutronization, accretion, and cooling SN phases), and $\langle E \rangle$, A_T are inferred by means of a maximum likelihood analysis, as described in the following.

We compute the total number of interactions N_{exp} (Eq. 5) for our *reference model* (27 M_\odot with LS220 EoS at 10 kpc) for the three RES-NOVA detector volumes, with 1 keV recoil energy threshold and 200 eV recoil energy resolution over the entire RoI:

$$N_{\text{exp}} = \int \frac{d^2 R}{dE_R dt} dt dE_R = \int \frac{dR}{dE_R} dE_R. \quad (10)$$

The probability density function for an event to induce a recoil of energy E_R is

$$p(E_R) = \frac{1}{N_{\text{exp}}} \frac{dR}{dE_R}. \quad (11)$$

A Monte Carlo dataset of the observable E_R is generated according to the distribution of Eq. 11 and the number of generated events (N_{obs}) is drawn from a Poisson distribution of average N_{exp} . The parametrization in Eq. 9 is used to write the extended likelihood: $\mathcal{L}(\langle E \rangle, N_{\text{exp}}(A_T); \{E_i\}_{i=1 \dots N_{\text{obs}}})$:

$$\ln \mathcal{L} = N_{\text{obs}} \ln(N_{\text{exp}}) - N_{\text{exp}} + \sum_{i=1}^{N_{\text{obs}}} \ln \tilde{p}(E_i) \quad (12)$$

with

$$\tilde{p}(E) = \frac{1}{N_{\text{exp}}} N_{Pb} A_T \int dE f^0(E; \langle E \rangle, \alpha_T) \frac{d\sigma}{dE_R}.$$

The parameter α_T is fixed to its time-average over the $[t_1, t_2]$ interval. The estimators for A_T and $\langle E \rangle$ are those maximizing the likelihood in Eq. 12; their 1σ confidence interval is obtained according to the Wilk's theorem, so that $2 \ln \mathcal{L}$ drops from its maximum by the quantile of a 2D χ^2 distribution evaluated at 68.26%.

The projected 1σ confidence contours of A_T and $\langle E \rangle$ for the three detector volumes are shown in Fig. 7. The parameter estimation is carried out for the three main phases of the neutrino emission for the 27 M_\odot SN model with LS220 EoS progenitor (top panels) and for the 40 M_\odot fast forming black hole collapse (bottom panels).

The maximum likelihood reconstructed values are shown together with their respective true values for each phase of the SN burst. The small discrepancy between the reconstructed and the true values is ascribed to the numerical accuracy of the calculation. The small number of expected events does not allow for a reliable reconstruction of the SN parameters for the neutronization burst of the 27 M_\odot SN model in RN¹ (< 3 counts). For this reason only the RN² and RN³ contour plots are shown. For the remaining two phases the statistics is large enough to enable an excellent parameter reconstruction with RN³. Note that the cooling phase has the longest duration among the different SN phases; as a consequence, the parametrization adopted in Eq. 9 is not accurate until 10 s, given the large variation of the neutrino emission properties within a long time interval. In order to produce reliable results, we only consider the first 7 s of the cooling phase, which carry most of the SN information.

For the fast black hole forming collapse, which is not featuring a cooling phase, only two contour plots are shown. The first one refers to the neutronization phase, and also in this case the expected statistics for RN¹ is too low to enable a meaningful parameter reconstruction. The second contour plot shows the calculation for [0.1, 0.25] s. This choice is driven by the fast change in time of the flux emission parameters, namely $\langle E \rangle$ and α_T (see Fig. 1). Hence, as already done for the cooling phase of the 27 M_\odot SN model we select a smaller time interval.

The reconstruction of the spectral parameters becomes extremely accurate as the detector volume increases. The SN true values for our input SN models (blue star) fall into the 1σ contour region for all the different RES-NOVA phases. The achievable precision on the estimation of the average neutrino energy and the neutrino fluence is competitive, and in some case better, than the

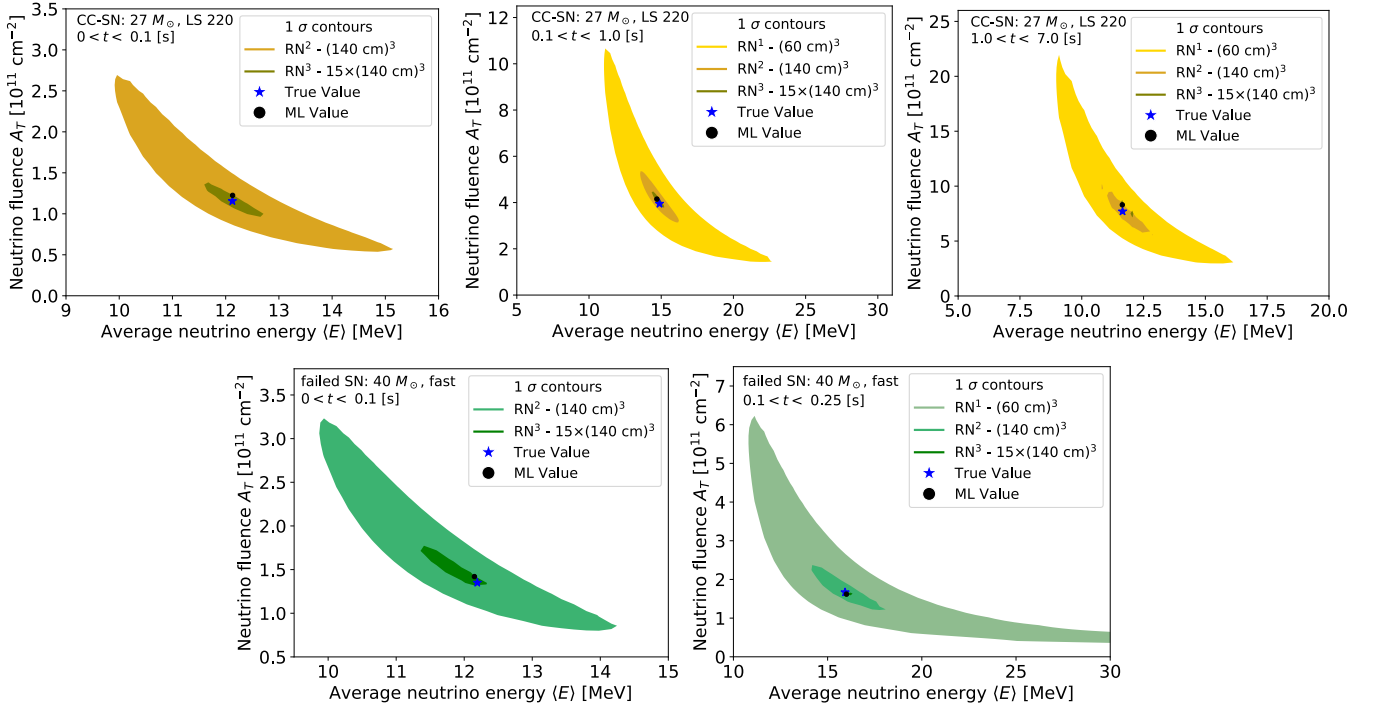


FIG. 7. Reconstructed average neutrino energy $\langle E \rangle$ and neutrino fluence A_T at the detector site (black dot) for the $27 M_{\odot}$ SN model with LS220 EoS progenitor (top panels) and for the $40 M_{\odot}$ fast black hole forming collapse (bottom panels). The investigated time intervals refer to the main SN phases: neutronization ($0 < t < 0.1$ s), accretion ($0.1 < t < 1$ s) and cooling ($1 < t < 7$ s) phases, expect for the black hole forming model which is not featuring a cooling phase. The true parameter values for the different phases of the two models are shown as blue stars. The color areas are the 1σ contours for mock experiments following our maximum likelihood analysis. The calculations are carried out for the three RES-NOVA phases: RN^1 , RN^2 , and RN^3 . The small statistics does not allow to achieve a good reconstruction of the SN parameters for the neutronization burst for both SN models in RN^1 ; hence, only the RN^2 and RN^3 contour plots are shown. The SN parameters will be measured with excellent precision with RN^3 .

values reconstructed for the Xenon detector in [36]. It should be stressed that our estimations rely on a very conservative assumption of the detector energy threshold of 1 keV, while the values assumed in [36] correspond to a threshold of about 0.5 keV. This is a significant difference in the neutrino statistics given that the spectral shape of the signal is expected to rise exponentially for lower nuclear recoil energies. Thus, RES-NOVA is able to achieve a precision on the estimation of the main SN parameters similar to the one of direct-detection dark matter experiments, but with less stringent constraints on the detector energy threshold. In addition, RES-NOVA has the advantage of being easily scalable to larger detector sizes.

We also estimate the total energy emitted by the SN in neutrinos:

$$\mathcal{E}_{\text{tot}} = 4\pi d^2 A_T \langle E \rangle. \quad (13)$$

In order to do that, we run 30 Monte Carlo simulations, for each detector volume, to determine the precision achievable in the reconstruction of \mathcal{E}_{tot} . The results are shown in Fig. 8, where the 1σ band for each Monte Carlo realization is plotted for each detector volume. For this estimation, we took into account the neutrino emission interval $[0, 10]$ s after the core bounce. The 1σ bands

are computed propagating the uncertainty on \mathcal{E}_{tot} and A_T in Eq. 13. The increase in the number of detected events shows a clear improvement in the precision of the \mathcal{E}_{tot} measure. The shape of the contours in Fig. 7 directly translates into a constraint on \mathcal{E}_{tot} in Fig. 8. The larger and irregular contours of the RN^1 and RN^2 phases result in broader and asymmetric bounds, when compared to RN^3 where the very large statistics makes \mathcal{E}_{tot} distributed according to a normal distribution. The achieved precision for the three RES-NOVA detectors is: 30%, 8%, 4%, for RN^1 , RN^2 and RN^3 , respectively.

D. Detection significance

The possibility to detect SN neutrinos from neighbouring galaxies can have a strong impact on the expected rate of SN observations. In fact, the larger is the number of galaxies under investigation the higher is the probability to observe a SN event. On the other hand, the farther are the galaxies the weaker is the expected signal in the detector, as it scales as d^{-2} . In Fig. 9 is shown the probability to detect at least 1 SN neutrino for our benchmark SN model ($27 M_{\odot}$ SN model with LS220 EoS) as a

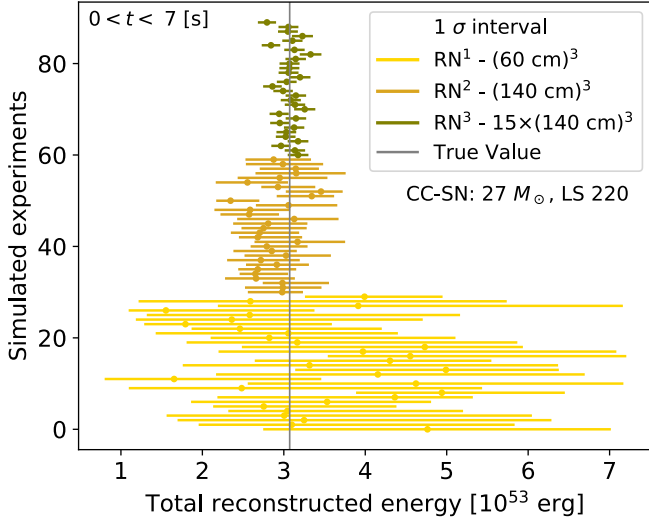


FIG. 8. Total reconstructed SN energy for the $27 M_{\odot}$ model with LS220 EoS, for a SN at 10 kpc. The circles represent the maximum likelihood value while the continuous horizontal lines represent the 1σ band. The yellow (bottom), brown (middle) and green (top) bands refer to the three RES-NOVA phases, RN^1 , RN^2 and RN^3 , respectively. The true value of the model is shown as a vertical line. The achieved precision for the three RES-NOVA detectors is: 30%, 8%, 4%, for RN^1 , RN^2 and RN^3 , respectively.

function of the SN distance. The detection significance is computed for the three RES-NOVA phases. On the same plot, on the right y-axis, is also shown the cumulative SN rate as from the Galaxy Catalog in [74].

We can infer that RN^1 is able to fully explore the Milky Way, RN^2 can reach out to the unexplored Andromeda, and RN^3 may potentially increase the expected rate of SN observations for the first time. RN^3 will be able to observe a SN event every ~ 3 yr with a probability of 0.2, thus to detect at least one event every ~ 10 yr. Having the possibility to investigate the SN rate over many galaxies is of utmost importance as it may shed light on the so-called SN rate problem [75].

V. DIFFUSE SUPERNOVA NEUTRINO BACKGROUND

A complementary approach to the detection of a single SN burst described in the previous section is the tantalizing possibility of pushing the SN neutrino detection to cosmological scales through the DSNB [5, 76, 77]. The DSNB has the potential to offer a glimpse on the overall SN population, opening a new epoch for extragalactic neutrino astronomy. After introducing our theoretical DSNB model, we investigate the DSNB detectability prospects with the RES-NOVA technology.

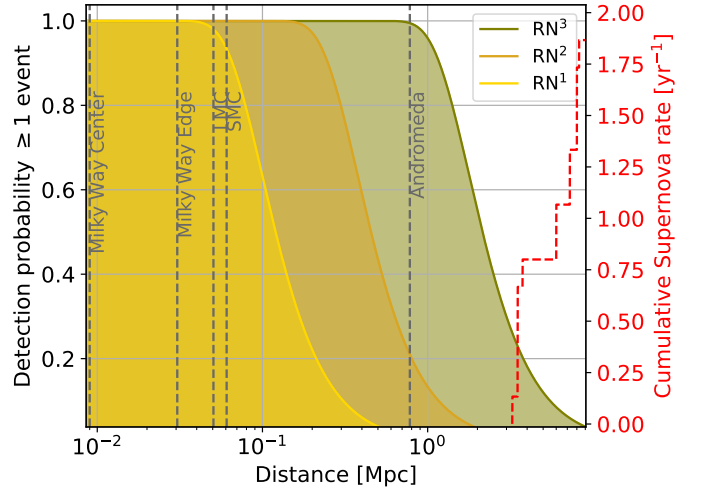


FIG. 9. Probability to detect at least 1 SN neutrino event as a function of the SN distance for our benchmark SN model ($27 M_{\odot}$ SN model with LS220 EoS). The shadowed areas represent the detection probability for the three different RES-NOVA phases: RN^1 , RN^2 , and RN^3 , respectively. The red dashed line shows the cumulative SN rate versus distance [74]. RN^3 will be able to detect at least one SN neutrino event every ~ 10 yr.

A. Theoretical inputs

The DSNB is an isotropic and stationary flux of neutrinos and anti-neutrinos produced by past SN events, both core-collapse SNe and failed SNe. The DSNB summed over all six flavors is defined in the following way:

$$\Phi(E) = \sum_{\beta} \frac{c}{H_0} \int_{8 M_{\odot}}^{125 M_{\odot}} dM \int_0^{\infty} dz \frac{R_{\text{SN}}(z, M)}{\sqrt{\Omega_M(1+z)^3 + \Omega_{\Lambda}}} \quad (14)$$

$$[f_{\text{CC-SN}} f_{\beta}^0[E(1+z), M] + f_{\text{failed-SN}} f_{\beta}^0[E(1+z), M]] ,$$

where M is the SN mass, $f_{\beta}^0[E(1+z), M]$ is the time-integrated neutrino flux for each SN progenitor of mass M (see Eq. 1), c is the speed of light, Ω_M and Ω_{Λ} are the matter and dark energy cosmic energy densities, H_0 is the Hubble constant, z is the redshift, and $R_{\text{SN}}(z, M)$ is the SN rate.

Current theoretical estimations of the DSNB lack of a comprehensive knowledge of the SN explosion mechanism. Moreover, the SN distribution as a function of the redshift is still uncertain. The most relevant uncertainties affecting the expected number of DSNB events concern the neutrino mass ordering, the fraction of failed and core-collapse SNe, and the uncertainties on the SN rate [78, 79].

In order to explore the RES-NOVA detector response to the DSNB signal, we take into account the maximal variation of the DSNB flux computed in Ref. [79] and shown in Fig. 10. The lower edge of the band in Fig. 10 was obtained for $f_{\text{failed-SN}} = 9\%$, $R_{\text{SN}}(z=0) = 0.75 \times 10^{-4} \text{ Mpc}^{-3} \text{ yr}^{-1}$, and by adopting the models with SFHo EoS for CC-SNe and the $40 M_{\odot}$ black hole collapse

model with fast accretion as representative of the failed SN population. The upper edge of the DSNB in Fig. 10 band was obtained by adopting $f_{\text{failed-SN}} = 0.41\%$, $R_{\text{SN}}(z=0) = 1.75 \times 10^{-4} \text{ Mpc}^{-3} \text{ yr}^{-1}$, and by adopting the models with LS220 EoS for CC-SNe and the $40 M_{\odot}$ black hole collapse model with slow accretion as representative of the failed SN population. We refer the interested reader to Ref. [79] for more details on the theoretical modeling.

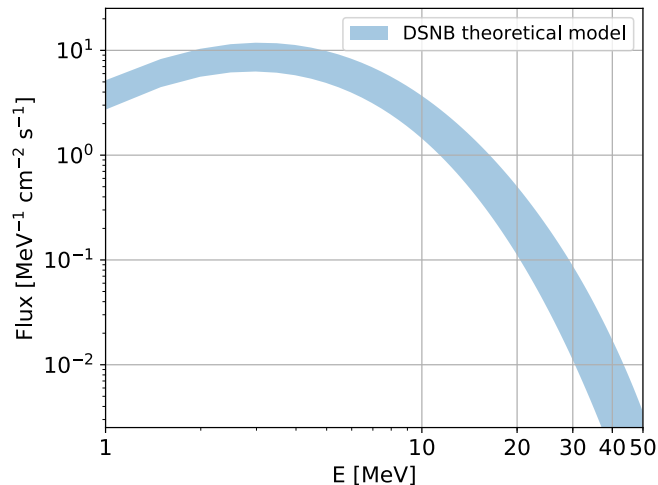


FIG. 10. DSNB for all six flavors as a function of the neutrino energy. The lower and upper bounds of the DSNB band were computed in Ref. [79], see text for details

B. Forecast of the DSNB recoil spectrum in RES-NOVA

Up to now, the DSNB has not been measured by any detector yet, nevertheless current experimental limits are very close to the theoretical upper limit. The Super-Kamiokande experiment established the most stringent limit on the $\bar{\nu}_e$ component of the DSNB flux: $> 2.8 - 3.1 \text{ cm}^{-2} \text{ s}^{-1}$ for neutrino energies above 17.3 MeV [80]. The likelihood of detecting the DSNB, however, is dramatically enhanced by the enrichment of Super-Kamiokande with Gadolinium [81] and by the upcoming JUNO [82]; see Refs. [79, 83] for forecasts of the DSNB detection potential with next-generation detectors.

RES-NOVA has the unique feature of being equally sensitive to all six neutrino flavors and will be especially sensitive to the high energy tail of the DSNB. The latter carries precious information on the fraction of failed SNe on cosmological scales [84]. Hence, even being a small scale detector, RES-NOVA could provide important complementary information.

Figure 11 shows the spectrum of the nuclear recoils induced by neutrino interactions obtained by adopting the DSNB spectrum displayed in Fig. 10. The DSNB recoil spectrum is normalized for the detector exposure (ton^{-1}

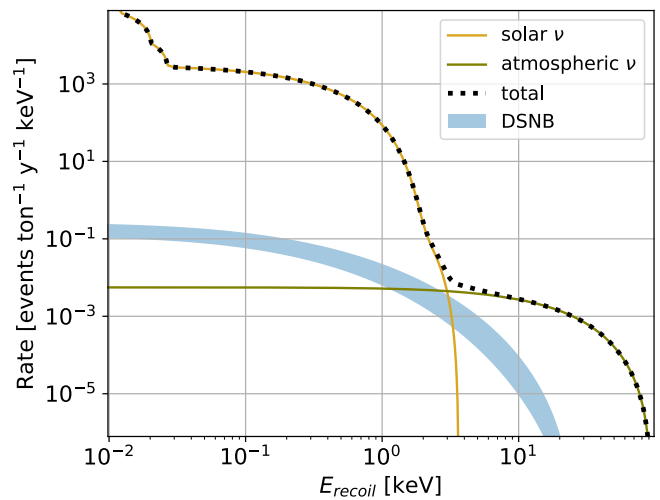


FIG. 11. Energy spectrum of nuclear recoils induced by neutrino interactions from different sources, per unit of detector exposure ($\text{ton}^{-1} \text{ yr}^{-1}$). The blue band represents the maximal variation of the DSNB flux according to the calculations of [79] (see Fig. 10), while the continuous lines refer to the solar and atmospheric neutrino fluxes [85, 86]. The dotted line is the detector response to the sum of the solar, atmospheric and maximal value of the DSNB fluxes.

yr^{-1}). The expected DSNB signal in RES-NOVA is weak, and for this reason a thorough background study is needed. On the same plot the expected signals from solar and atmospheric neutrino backgrounds as from [85, 86] are also shown. The DSNB signal is overwhelmed by the solar neutrino component, mainly ^8B , in the lower energy region (up to $\sim 3 \text{ keV}$). While at higher recoil energies the atmospheric background becomes dominant. On the other hand, we neglect the detector intrinsic background (e.g., β/γ 's from ^{210}Pb in archaeological Pb) and the external neutron one (e.g. cosmic ray induced neutrons). The first background can be lowered to a negligible level by means of particle identification techniques both on pure-Pb detectors [87] as well as on Pb-based compounds [54, 64]. The second one can be suppressed by means of a highly efficient veto around the experimental set-up, as already done in dark matter experiments [88].

If we assume a detector energy threshold of 1 keV and to collect $620 \text{ ton}^{-1} \text{ yr}^{-1}$ of exposure, which corresponds to operate RN² for 20 yr, we will observe about 15 DSNB events above the irreducible background of solar and atmospheric neutrinos. Such a rate is competitive and complementary to the one expected in facilities of tens of kilotons in mass, which use water, liquid Ar, and liquid scintillator [79, 89].

VI. CONCLUSIONS

RES-NOVA is an innovative research program based on the detection of supernova neutrinos using archae-

ological lead cryogenic detectors, exploiting the coherent elastic neutrino-nucleus scattering (CE ν NS). RES-NOVA can potentially allow for a comprehensive exploration of the most relevant supernova parameters.

The cryogenic technology together with the ultra-low radioactivity of archaeological lead enable the achievement of excellent detector performance in terms of energy threshold, energy resolution and background level in the region of interest. In addition, RES-NOVA can achieve a high statistics detection of all neutrino flavors emitted by a supernova, thanks to the high CE ν NS cross-section, which is some orders of magnitude higher than the conventional detection channels.

The innovative approach of RES-NOVA allows for a major detector miniaturization compared to all other neutrino detectors, without extreme detector performance (e.g., energy threshold). Intriguingly, the modular RES-NOVA technology enables an easy detector volume scaling, without technological development, unlike all other technologies (water Cherenkov, liquid scintillator and noble-liquid time projection chambers) which run monolithic detectors.

The scalability of the proposed technology to larger detector volumes facilitates a broad research program. In the first detector phase, a thorough investigation of the entire Milky Way can be carried out; while in the second and third phases, our search can potentially reach neighbouring galaxies. The increase in the detector volume guarantees large neutrino statistics, and thus to achieve a precision up to 4% on the estimation of the total energy

carried supernova neutrinos.

The original experimental approach described in this work also grants sensitivity to the diffuse supernova neutrino background with a modest detector exposure. In fact, with only 620 ton⁻¹ yr⁻¹ of exposure and a detector energy threshold of 1 keV, RES-NOVA can detect about 15 events above the irreducible background of solar and atmospheric neutrinos.

The RES-NOVA experiment will complement currently running neutrino detectors, thanks to the high cross-section of the exploited CE ν NS channel. In addition, the miniaturization of the detector, and its easy scalability promise to pioneer a new generation of neutrino telescopes.

ACKNOWLEDGMENTS

We are grateful to Georg Raffelt and Francesco Vissani for useful discussions. This research was supported by the Excellence Cluster ORIGINS which is funded by the Deutsche Forschungsgemeinschaft (DFG, German Research Foundation) under Germany's Excellence Strategy EXC-2094 390783311, the Villum Foundation (Project No. 13164), the Danmarks Frie Forskningsfonds (Project No. 8049-00038B), the Knud Højgaard Foundation, and the Deutsche Forschungsgemeinschaft through Sonderforschungsbereich SFB 1258 "Neutrinos and Dark Matter in Astro- and Particle Physics" (NDM).

-
- [1] H.-T. Janka, K. Langanke, A. Marek, G. Martínez-Pinedo, and B. Müller, *Phys. Rept.* **442**, 38 (2007), [arXiv:astro-ph/0612072 \[astro-ph\]](#).
 - [2] A. Burrows, *Rev. Mod. Phys.* **85**, 245 (2013), [arXiv:1210.4921 \[astro-ph.SR\]](#).
 - [3] H.-T. Janka, T. Melson, and A. Summa, *Ann. Rev. Nucl. Part. Sci.* **66**, 341 (2016), [arXiv:1602.05576 \[astro-ph.SR\]](#).
 - [4] B. Müller, *Ann. Rev. Nucl. Part. Sci.* **69**, 253 (2019), [arXiv:1904.11067 \[astro-ph.HE\]](#).
 - [5] A. Mirizzi, I. Tamborra, H.-T. Janka, N. Saviano, K. Scholberg, R. Bollig, L. Hüdepohl, and S. Chakraborty, *Riv. Nuovo Cim.* **39**, 1 (2016), [arXiv:1508.00785 \[astro-ph.HE\]](#).
 - [6] S. Horiuchi and J. P. Kneller, *J. Phys. G* **45**, 043002 (2018), [arXiv:1709.01515 \[astro-ph.HE\]](#).
 - [7] S. Shalgar, I. Padilla-Gay, and I. Tamborra, (2019), [arXiv:1911.09110 \[astro-ph.HE\]](#).
 - [8] S. Shalgar, I. Tamborra, and M. Bustamante, (2019), [arXiv:1912.09115 \[astro-ph.HE\]](#).
 - [9] A. M. Suliga, I. Tamborra, and M.-R. Wu, *JCAP* **1912**, 019 (2019), [arXiv:1908.11382 \[astro-ph.HE\]](#).
 - [10] L. Mastrototaro, A. Mirizzi, P. D. Serpico, and A. Esmaili, *JCAP* **2001**, 010 (2020), [arXiv:1910.10249 \[hep-ph\]](#).
 - [11] A. Sung, H. Tu, and M.-R. Wu, *Phys. Rev. D* **99**, 121305 (2019), [arXiv:1903.07923 \[hep-ph\]](#).
 - [12] M.-R. Wu, T. Fischer, L. Huther, G. Martínez-Pinedo, and Y.-Z. Qian, *Phys. Rev. D* **89**, 061303 (2014), [arXiv:1305.2382 \[astro-ph.HE\]](#).
 - [13] A. de Gouvêa, I. Martínez-Soler, and M. Sen, *Phys. Rev. D* **101**, 043013 (2020), [arXiv:1910.01127 \[hep-ph\]](#).
 - [14] C. J. Stapleford, D. J. Väänänen, J. P. Kneller, G. C. McLaughlin, and B. T. Shapiro, *Phys. Rev. D* **94**, 093007 (2016), [arXiv:1605.04903 \[hep-ph\]](#).
 - [15] A. Esteban-Pretel, R. Tomas, and J. W. F. Valle, *Phys. Rev. D* **76**, 053001 (2007), [arXiv:0704.0032 \[hep-ph\]](#).
 - [16] A. Drukier and L. Stodolsky, *Phys. Rev. D* **30**, 2295 (1984), [[395\(1984\)](#)].
 - [17] J. F. Beacom, W. M. Farr, and P. Vogel, *Phys. Rev. D* **66**, 033001 (2002), [arXiv:hep-ph/0205220 \[hep-ph\]](#).
 - [18] C. J. Horowitz, K. J. Coakley, and D. N. McKinsey, *Phys. Rev. D* **68**, 023005 (2003), [arXiv:astro-ph/0302071 \[astro-ph\]](#).
 - [19] K. Scholberg, *J. Phys. G* **45**, 014002 (2018), [arXiv:1707.06384 \[hep-ex\]](#).
 - [20] K. Asakura *et al.* (KamLAND), *Astrophys. J.* **818**, 91 (2016), [arXiv:1506.01175 \[astro-ph.HE\]](#).
 - [21] L. Cadonati, F. P. Calaprice, and M. C. Chen, *Astropart. Phys.* **16**, 361 (2002), [arXiv:hep-ph/0012082 \[hep-ph\]](#).
 - [22] N. Yu. Agafonova *et al.*, *Astropart. Phys.* **27**, 254 (2007), [arXiv:hep-ph/0609305 \[hep-ph\]](#).
 - [23] F. An *et al.* (Juno), *Journal of Physics G: Nuclear and Particle Physics* **43**, 030401 (2016).

- [24] M. R. Vagins, *J. Phys. Conf. Ser.* **1216**, 012008 (2019).
- [25] A. Gallo Rosso, F. Vissani, and M. C. Volpe, *JCAP* **1804**, 040 (2018), [arXiv:1712.05584 \[hep-ph\]](#).
- [26] R. Abbasi *et al.* (IceCube), *Astron. Astrophys.* **535**, A109 (2011), [Erratum: *Astron. Astrophys.* 563, C1(2014)], [arXiv:1108.0171 \[astro-ph.HE\]](#).
- [27] J. Migenda (DUNE), in *Proceedings, Prospects in Neutrino Physics (NuPhys2017): London, UK, December 20-22, 2017* (2018) pp. 164–168, [arXiv:1804.01877 \[physics.ins-det\]](#).
- [28] K. Scholberg, *Ann. Rev. Nucl. Part. Sci.* **62**, 81 (2012), [arXiv:1205.6003 \[astro-ph.IM\]](#).
- [29] B. Dasgupta and J. F. Beacom, *Phys. Rev.* **D83**, 113006 (2011), [arXiv:1103.2768 \[hep-ph\]](#).
- [30] E. Kolbe and K. Langanke, *Phys. Rev.* **C63**, 025802 (2001), [arXiv:nucl-th/0003060 \[nucl-th\]](#).
- [31] C. Volpe, N. Auerbach, G. Colo, and N. Van Giai, *Phys. Rev.* **C65**, 044603 (2002), [arXiv:nucl-th/0103039 \[nucl-th\]](#).
- [32] D. Väänänen and C. Volpe, *JCAP* **1110**, 019 (2011), [arXiv:1105.6225 \[astro-ph.SR\]](#).
- [33] D. Z. Freedman, D. N. Schramm, and D. L. Tubbs, *Ann. Rev. Nucl. Part. Sci.* **27**, 167 (1977).
- [34] D. Akimov *et al.* (COHERENT), *Science* **357**, 1123 (2017), [arXiv:1708.01294 \[nucl-ex\]](#).
- [35] T. Marrodán Undagoitia and L. Rauch, *J. Phys.* **G43**, 013001 (2016), [arXiv:1509.08767 \[physics.ins-det\]](#).
- [36] R. F. Lang, C. McCabe, S. Reichard, M. Selvi, and I. Tamborra, *Phys. Rev.* **D94**, 103009 (2016), [arXiv:1606.09243 \[astro-ph.HE\]](#).
- [37] J. L. Newstead, R. F. Lang, and L. E. Strigari, (2020), [arXiv:2002.08566 \[astro-ph.CO\]](#).
- [38] J. Monroe and P. Fisher, *Phys. Rev.* **D76**, 033007 (2007), [arXiv:0706.3019 \[astro-ph\]](#).
- [39] L. E. Strigari, *New J. Phys.* **11**, 105011 (2009), [arXiv:0903.3630 \[astro-ph.CO\]](#).
- [40] K. Abe *et al.* (XMASS), *Astropart. Phys.* **89**, 51 (2017), [arXiv:1604.01218 \[physics.ins-det\]](#).
- [41] I. Tamborra, B. Müller, L. Hüpdepohl, H.-T. Janka, and G. G. Raffelt, *Phys. Rev.* **D86**, 125031 (2012), [arXiv:1211.3920 \[astro-ph.SR\]](#).
- [42] M. T. Keil, G. G. Raffelt, and H.-T. Janka, *Astrophys. J.* **590**, 971 (2003), [arXiv:astro-ph/0208035 \[astro-ph\]](#).
- [43] MPA Supernova Archive, <https://www.mpa.mpg.de/ccsnarchive>, <https://www.mpa.mpg.de/ccsnarchive/data/>.
- [44] J. M. Lattimer and F. D. Swesty, *Nucl. Phys.* **A535**, 331 (1991).
- [45] A. W. Steiner, M. Hempel, and T. Fischer, *Astrophys. J.* **774**, 17 (2013), [arXiv:1207.2184 \[astro-ph.SR\]](#).
- [46] E. O'Connor *et al.*, *J. Phys.* **G45**, 104001 (2018), [arXiv:1806.04175 \[astro-ph.HE\]](#).
- [47] I. Tamborra, G. G. Raffelt, F. Hanke, H.-T. Janka, and B. Müller, *Phys. Rev.* **D90**, 045032 (2014), [arXiv:1406.0006 \[astro-ph.SR\]](#).
- [48] L. Walk, I. Tamborra, H.-T. Janka, and A. Summa, (2019), [arXiv:1910.12971 \[astro-ph.HE\]](#).
- [49] S. Chakraborty, R. Hansen, I. Izaguirre, and G. G. Raffelt, *Nucl. Phys.* **B908**, 366 (2016), [arXiv:1602.02766 \[hep-ph\]](#).
- [50] E. W. Kolb and M. S. Turner, *Phys. Rev. D* **36**, 2895 (1987).
- [51] E. W. Kolb and M. S. Turner, *Phys. Rev. Lett.* **62**, 509 (1989).
- [52] R. H. Helm, *Phys. Rev.* **104**, 1466 (1956).
- [53] C. J. Horowitz, Z. Ahmed, C.-M. Jen, A. Rakhman, P. A. Souder, M. M. Dalton, N. Liyanage, K. D. Paschke, K. Saenboonruang, R. Silwal, G. B. Franklin, M. Friend, B. Quinn, K. S. Kumar, D. McNulty, L. Mercado, S. Riordan, J. Wexler, R. W. Michaels, and G. M. Urciuoli, *Phys. Rev. C* **85**, 032501 (2012).
- [54] J. W. Beeman *et al.*, *Eur. Phys. J.* **A49**, 50 (2013), [arXiv:1212.2422 \[nucl-ex\]](#).
- [55] A. H. Abdelhameed *et al.* (CRESST), *Phys. Rev.* **D100**, 102002 (2019), [arXiv:1904.00498 \[astro-ph.CO\]](#).
- [56] K. Alfonso *et al.* (CUORE), *Phys. Rev. Lett.* **115**, 102502 (2015), [arXiv:1504.02454 \[nucl-ex\]](#).
- [57] F. Alessandria *et al.*, *JCAP* **1301**, 038 (2013), [arXiv:1209.2519 \[physics.ins-det\]](#).
- [58] C. Alduino *et al.* (CUORE), *Phys. Rev. Lett.* **120**, 132501 (2018), [arXiv:1710.07988 \[nucl-ex\]](#).
- [59] N. Casali *et al.*, *J. Phys.* **G41**, 075101 (2014), [arXiv:1311.2834 \[nucl-ex\]](#).
- [60] J. W. Beeman *et al.*, *Phys. Rev. Lett.* **108**, 062501 (2012), [arXiv:1110.3138 \[nucl-ex\]](#).
- [61] L. Pattavina, M. Laubenstein, S. S. Nagorny, S. Nisi, L. Pagnanini, S. Pirro, C. Rusconi, and K. Schöffner, *Eur. Phys. J.* **A54**, 79 (2018), [arXiv:1801.03980 \[physics.ins-det\]](#).
- [62] O. Azzolini *et al.* (CUPID), *Phys. Rev. Lett.* **123**, 032501 (2019), [arXiv:1906.05001 \[nucl-ex\]](#).
- [63] L. Pattavina, J. W. Beeman, M. Clemenza, O. Cremonesi, E. Fiorini, L. Pagnanini, S. Pirro, C. Rusconi, and K. Schffner, *Eur. Phys. J.* **A55**, 127 (2019), [arXiv:1904.04040 \[physics.ins-det\]](#).
- [64] L. Pattavina, S. Nagorny, S. Nisi, L. Pagnanini, G. Pessina, S. Pirro, C. Rusconi, K. Schöffner, V. N. Shlegel, and V. N. Zhidankov, *Eur. Phys. J.* **A56**, 38 (2020).
- [65] C. Alduino *et al.*, *Cryogenics* **102**, 9 (2019), [arXiv:1904.05745 \[physics.ins-det\]](#).
- [66] E. Armengaud *et al.* (EDELWEISS), *Phys. Rev.* **D99**, 082003 (2019), [arXiv:1901.03588 \[astro-ph.GA\]](#).
- [67] R. Agnese *et al.* (SuperCDMS), *Phys. Rev.* **D97**, 022002 (2018), [arXiv:1707.01632 \[astro-ph.CO\]](#).
- [68] O. Azzolini *et al.* (CUPID), *Eur. Phys. J.* **C78**, 428 (2018), [arXiv:1802.06562 \[physics.ins-det\]](#).
- [69] S. Pirro and P. Mauskopf, *Ann. Rev. Nucl. Part. Sci.* **67**, 161 (2017).
- [70] F. Alessandria *et al.*, *Astropart. Phys.* **45**, 13 (2013), [arXiv:1210.1107 \[nucl-ex\]](#).
- [71] P. Giampa (DEAP-3600), *Proceedings, 6th Topical Workshop on Low Radioactivity Techniques (LRT 2017): Seoul, Korea, May 24-26, 2017*, *AIP Conf. Proc.* **1921**, 070005 (2018).
- [72] C. Alduino *et al.* (CUORE), *Eur. Phys. J.* **C77**, 543 (2017), [arXiv:1704.08970 \[physics.ins-det\]](#).
- [73] G. Heusser, M. Laubenstein, and H. Nader, in *Radionuclides in the Environment*, Radioactivity in the Environment, Vol. 8, edited by P. Povinec and J. Sanchez-Cabeza (Elsevier, 2006) pp. 495 – 510.
- [74] I. D. Karachentsev, V. E. Karachentseva, W. K. Huchtmeier, and D. I. Makarov, *Astron. J.* **127**, 2031 (2004).
- [75] S. Horiuchi, J. F. Beacom, C. S. Kochanek, J. L. Prieto, K. Z. Stanek, and T. A. Thompson, *Astrophys. J.* **738**, 154 (2011), [arXiv:1102.1977 \[astro-ph.CO\]](#).
- [76] J. F. Beacom, *Ann. Rev. Nucl. Part. Sci.* **60**, 439 (2010), [arXiv:1004.3311 \[astro-ph.HE\]](#).

- [77] C. Lunardini, *Astropart. Phys.* **79**, 49 (2016), [arXiv:1007.3252 \[astro-ph.CO\]](#).
- [78] C. Lunardini and I. Tamborra, *JCAP* **1207**, 012 (2012), [arXiv:1205.6292 \[astro-ph.SR\]](#).
- [79] K. Møller, A. M. Suliga, I. Tamborra, and P. B. Denton, *JCAP* **1805**, 066 (2018), [arXiv:1804.03157 \[astro-ph.HE\]](#).
- [80] K. Bays *et al.* (Super-Kamiokande), *Phys. Rev.* **D85**, 052007 (2012), [arXiv:1111.5031 \[hep-ex\]](#).
- [81] T. Mori (Super-Kamiokande), *Nucl. Instrum. Meth. A* **732**, 316 (2013).
- [82] F. An *et al.* (JUNO), *J. Phys.* **G43**, 030401 (2016), [arXiv:1507.05613 \[physics.ins-det\]](#).
- [83] A. Priya and C. Lunardini, *JCAP* **1711**, 031 (2017), [arXiv:1705.02122 \[astro-ph.HE\]](#).
- [84] C. Lunardini, *Phys. Rev. Lett.* **102**, 231101 (2009), [arXiv:0901.0568 \[astro-ph.SR\]](#).
- [85] Solar neutrino data, <http://www.sns.ias.edu/~jnb/SNdata/sndata.html>, <http://www.sns.ias.edu/~jnb/SNdata/sndata.html>.
- [86] G. Battistoni, A. Ferrari, T. Montaruli, and P. Sala, *Astropart. Phys.* **19**, 269 (2003), [Erratum: *Astropart. Phys.* **19**, 291–294 (2003)], [arXiv:hep-ph/0207035](#).
- [87] N. E. Booth and D. J. Goldie, *Superconductor Science and Technology* **9**, 493 (1996).
- [88] E. A. et al., *Journal of Instrumentation* **9**, P11006 (2014).
- [89] C. Lunardini, in *Handbook of Supernovae*, Radioactivity in the Environment, edited by A. Alsabti and P. Murdin (Springer, 2016) pp. 1 – 17.